



저작자표시-비영리-변경금지 2.0 대한민국

이용자는 아래의 조건을 따르는 경우에 한하여 자유롭게

- 이 저작물을 복제, 배포, 전송, 전시, 공연 및 방송할 수 있습니다.

다음과 같은 조건을 따라야 합니다:



저작자표시. 귀하는 원저작자를 표시하여야 합니다.



비영리. 귀하는 이 저작물을 영리 목적으로 이용할 수 없습니다.



변경금지. 귀하는 이 저작물을 개작, 변형 또는 가공할 수 없습니다.

- 귀하는, 이 저작물의 재이용이나 배포의 경우, 이 저작물에 적용된 이용허락조건을 명확하게 나타내어야 합니다.
- 저작권자로부터 별도의 허가를 받으면 이러한 조건들은 적용되지 않습니다.

저작권법에 따른 이용자의 권리는 위의 내용에 의하여 영향을 받지 않습니다.

이것은 [이용허락규약\(Legal Code\)](#)을 이해하기 쉽게 요약한 것입니다.

[Disclaimer](#)

공학석사학위논문

**Ce-Incorporated Yolk-Shell LaFeO<sub>3</sub>  
Perovskite Oxide as an Efficient Catalyst  
for NH<sub>3</sub>-SCR of Nitric Oxides**

세륨 및 요크-셸 구조 도입을 통해  
촉매 성능 및 내구성이 향상된 페로브스카이트 산화물  
기반 탈질 촉매에 대한 연구

2020년 2월

서울대학교 대학원  
재료공학부  
원 대 연

# Abstract

## **Ce-Incorporated Yolk-Shell LaFeO<sub>3</sub> Perovskite Oxide as an Efficient Catalyst for NH<sub>3</sub>-SCR of Nitric Oxides**

Dae-Yeon Won

Department of Materials Science and Engineering

The Graduate School

Seoul National University

Control of compositional and morphological structures is important to enhance catalytic performance and stability. In this work, we utilized this strategy to synthesize cerium-incorporated LaFeO<sub>3</sub> oxides and finally demonstrated cerium-substituted LaFeO<sub>3</sub> yolk-shell microspheres as efficient catalysts for selective catalytic reduction (SCR) of nitrogen oxides (NO<sub>x</sub>).

First, amorphous and citrate-chelated microspheres were synthesized by Pluronic F127-assisted hydrothermal treatment, followed by calcination to crystallize their perovskite structure. Cerium ions were substituted during

hydrothermal process or impregnated as oxide forms on LaFeO<sub>3</sub> microspheres. Then, samples prepared by various compositions and experimental conditions were thoroughly characterized with appropriate tools.

Particularly, when Ce ions substituted La ions, the substituted sample, LCFO, exhibited suitable chemical structure for SCR catalysts such as high concentration of Ce<sup>3+</sup> ions and surface oxygen species. In addition, heterogeneous contraction could be applied to LCFO by controlling calcination process; as a result, we could obtain LCFO with yolk-shell morphology (yLCFO). yLCFO showed a superior SCR performance over a wide range of operating temperature and SO<sub>2</sub> resistance. In conclusion, a LaFeO<sub>3</sub>-based efficient SCR catalyst was successfully developed by compositional and morphological control. It is expected that yLCFO could be a promising candidate as an alternative catalyst for SCR of nitrogen oxides.

## **Keywords**

LaFeO<sub>3</sub> perovskite oxides, Cerium incorporation, Nitrogen oxides (NO<sub>x</sub>), Selective catalytic reduction (SCR), Heterogeneous contraction, Yolk-shell structure

***Student number: 2015-20847***

# Contents

<b>ABSTRACT</b> .....	<b>i</b>
<b>CONTENTS</b> .....	<b>iii</b>
<b>1. Introduction</b> .....	<b>1</b>
<b>2. Experimental</b> .....	<b>8</b>
2.1. Materials .....	8
2.2. Synthesis of LaFeO <sub>3</sub> perovskite oxides .....	9
2.3. Synthesis of Ce-impregnated LaFeO <sub>3</sub> (CLFO series) catalysts.....	11
2.4. Synthesis of Ce-substituted LaFeO <sub>3</sub> (LCFO series) catalysts.....	13
2.5. Synthesis of yolk-shell structured LCFO catalysts .....	13
2.6. Catalyst characterization.....	14
2.7. Catalyst performance tests .....	16
<b>3. Results and discussion</b> .....	<b>18</b>
3.1. LaFeO <sub>3</sub> perovskite oxide microspheres .....	18
3.1.1. Crystal structure .....	18
3.1.2. Morphological and textural structure.....	20
3.1.3. The effect of calcination temperature .....	23
3.2. Ce-incorporated LaFeO <sub>3</sub> catalysts .....	25
3.2.1. Crystal structure .....	25

3.2.2. Morphological and textural structure.....	27
3.2.3. Surface chemical structure.....	33
3.2.4. NH <sub>3</sub> -SCR performance.....	38
3.3. Yolk-shell structured LCFO.....	43
3.3.1. Morphological structure.....	43
3.3.2. NH <sub>3</sub> -SCR performance.....	47
3.3.3. SO <sub>2</sub> resistance.....	50
<b>4. Conclusion.....</b>	<b>55</b>
<b>5. References.....</b>	<b>56</b>
<b>6. Korean ABSTRACT.....</b>	<b>65</b>

# 1. Introduction

Air pollution is defined as the emission of harmful substances to the atmosphere, which include a number of pollutants such as sulfur dioxide (SO<sub>2</sub>), nitrogen oxides (NO<sub>x</sub>), ozone (O<sub>3</sub>), particulate matter (PM) and volatile organic compounds (VOCs).<sup>1</sup> It has caused serious problems about human health and natural environment in modern days. And the pollutants are complicatedly related to the environmental outcomes, which makes disentanglement of specific pollutant very difficult. Therefore, purification or reduction of emission every pollutant should be considered importantly.

NO<sub>x</sub>, a generic term for compounds composed of N and O, are generated from combustion of N-containing fuel, and closely related to various environmental problems which can be formidable threats to public health (**Figure 1**).<sup>2,3,4</sup> For examples, NO<sub>x</sub> emitted to air is one of the major substances of secondary PM<sub>2.5</sub> (PM with a diameter less than 2.5 μm) formation, has large impacts on the ozone depletion, and deteriorates ecosystems through acid rain and eutrophication etc. In addition, NO<sub>x</sub> species provoke respiratory diseases like pneumonia and is classified as a cancer-causing substance since 2012. NO<sub>x</sub> emission mainly occurs in mobile and industrial fields (**Figure 2**). As a results, a lot of researches have been conducted to reduce NO<sub>x</sub> generated from these two sources.

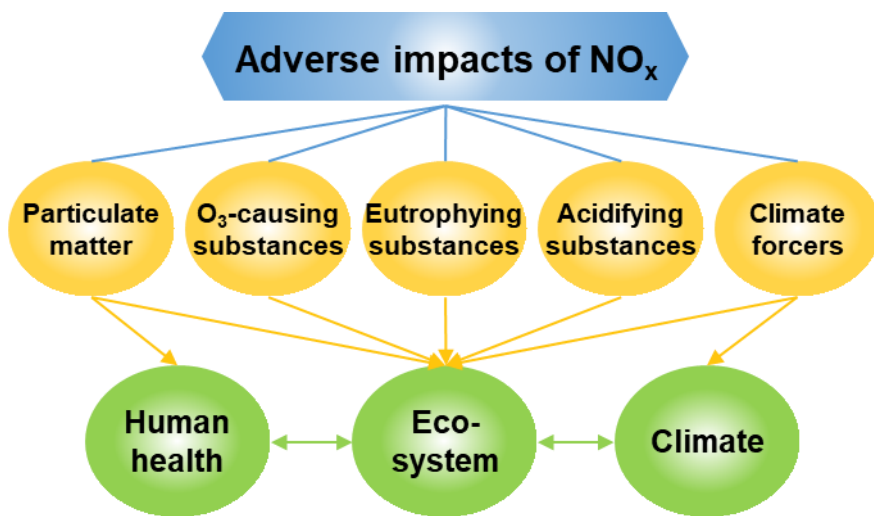


**Figure 1.** Adverse impacts of the emitted  $\text{NO}_x$

## Emission sources

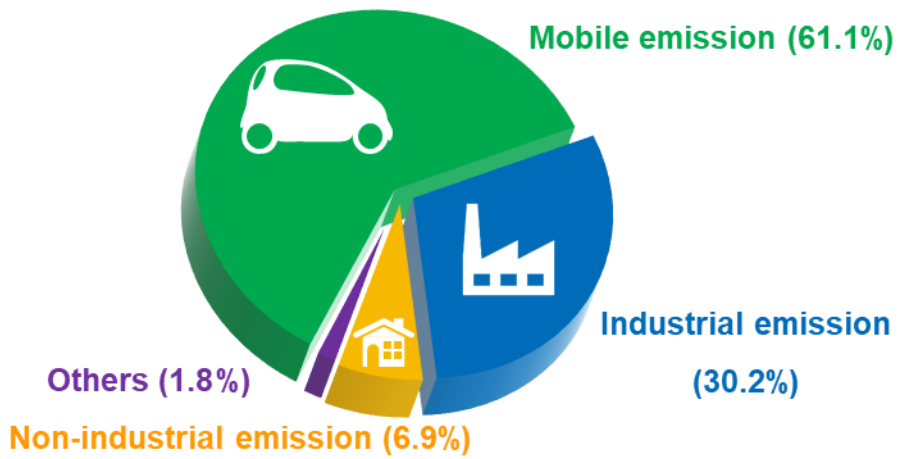
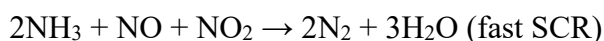


**Figure 2.** Emission sources of the NO<sub>x</sub>

To meet the stringent regulation of NO<sub>x</sub> emission, post-combustion processes have been utilized because other processes like denitrification of fuel and combustion control are not sufficient.<sup>5</sup> Selective catalytic reduction with ammonia (NH<sub>3</sub>-SCR) is the most widely used technology for NO<sub>x</sub> abatement due to its outstanding efficiency among the post-combustion denitrification processes. In NH<sub>3</sub>-SCR, NO<sub>x</sub> is converted into non-toxic gases, N<sub>2</sub> and H<sub>2</sub>O, by catalytic reaction with NH<sub>3</sub>, and the main reactions as follows:<sup>6,7</sup>



The catalyst is the key element in the SCR technique to determine overall efficiency, operating temperature, and lifespan of the system. Noble metal-based catalysts utilized for initial SCR system were not suitable because of instability of ammonium nitrate in the operation temperature. Through advancement of the technology, most of present NH<sub>3</sub>-SCR systems are comprised of vanadium-based catalysts such as V<sub>2</sub>O<sub>5</sub>-WO<sub>3</sub>/TiO<sub>2</sub>. However, V-based catalysts have a lack of high thermal durability and SO<sub>2</sub> resistance due to a high catalyzing potential to oxidize SO<sub>2</sub> into SO<sub>3</sub>, which makes the catalysts deteriorated during long-term operation.<sup>8</sup> Therefore, there have been steady demands for the development of suitable deNO<sub>x</sub> catalysts with thermal

stability and SO<sub>2</sub> resistance to endure continuous exposure of high temperature and SO<sub>2</sub> gas.

Lanthanum-based perovskite oxides with the chemical formula LaMO<sub>3</sub> have emerged as an important class of material because of their exceptional thermal stability, crystal structure, optical properties and redox behavior.<sup>9,10</sup> As the perovskite band structure offers considerable flexibility by substitution of metal cation sites, these materials have become promising candidates in a wide variety of catalytic reactions. In addition to catalytic activity, perovskites also demonstrate exceptional thermal stability, which is a very important property with respect to the long-term stability of the catalysts.<sup>11</sup> However, perovskite oxides suffer from low surface areas resulting from the high temperature calcination during LaMO<sub>3</sub> synthesis. Furthermore, their catalytic activities for NH<sub>3</sub>-SCR are not sufficient and SO<sub>2</sub> tolerance is poor.<sup>12,13</sup> Therefore, it is necessary to overcome these inherent limitations in order to expand the application fields of the catalysts.

Tuning compositional and morphological structure of catalysts is an important factor to improve the inherent catalytic properties. Especially, selection of an appropriate doping element could affect the morphological change, which, in some cases, results in an increased catalytic performance. Cerium could be considered as the dopant for lanthanum-based perovskite

oxides because Ce has been reported to facilitate of NH<sub>3</sub>-SCR catalysts owing to its distinctive redox and oxygen storage properties. It has been reported that cerium can act as a promoter to improve the SCR performance and SO<sub>2</sub> tolerance.<sup>14,15</sup> Besides, Ce cations have proper ionic radii and valence states to substitute La<sup>3+</sup> cation sites of perovskite oxides (Ce<sup>3+</sup>, 148 pm; Ce<sup>4+</sup>, 128 pm; La<sup>3+</sup>, 150 pm).<sup>16</sup> On the other hand, yolk-shell structure, a special class of core-shell structure with core@void@shell configuration, has unique properties contributed to movable cores and hollow space between core and shell, which leads to improvement of physical and chemical properties.<sup>17-19</sup> Based on its distinctive structure and properties, yolk-shell structured materials have drawn tremendous attention in various catalytic applications. Especially, formation of hollow void between movable core and shell unblocks surfaces of the core and the inner shell, and makes materials more suitable to accommodate the reactants resulting in a reactant-rich microenvironment. Yolk-shell structures have been prepared by a variety of methods e.g. hard-soft templating, galvanic replacement or heterogeneous contraction, and most of these preparation processes are affected by composition of precursors.<sup>20-22</sup> Thus, it is expected that cerium incorporation into perovskite oxides may also improve their catalytic activity and chemical resistance.

Accordingly, the strategy herein is to promote synergistic effects between Ce-incorporation and yolk-shell structure to enhance catalytic performance and SO<sub>2</sub> resistance of perovskite oxides as SCR catalysts. For this purpose, thermally stable Ce-substituted LaFeO<sub>3</sub> perovskite-type oxides having spherical morphology and yolk-shell structures were synthesized, their physical and chemical properties were characterized, and finally NH<sub>3</sub>-SCR catalytic performance and SO<sub>2</sub> resistance were investigated.

## 2. Experimental

### 2.1. Materials

Lanthanum (III) nitrate hexahydrate ( $\text{La}(\text{NO}_3)_3 \cdot 6\text{H}_2\text{O}$ , 99.9%) and citric acid (99%) were obtained from Alfa-Aesar Co. Ltd. (USA). Iron (III) nitrate nonahydrate ( $\text{Fe}(\text{NO}_3)_3 \cdot 9\text{H}_2\text{O}$ , 99%) was purchased from Daejung Chemical & Metals Co., Ltd. (Korea). Cerium (III) nitrate hexahydrate ( $\text{Ce}(\text{NO}_3)_3 \cdot 6\text{H}_2\text{O}$ , 99%) and poly(ethylene oxide)–poly(propylene oxide)–poly(ethylene oxide) tri-block copolymer (Pluronic F127,  $M_w = 12,600$  g/mol) were obtained from Sigma-Aldrich Co., Inc. (USA). Ethyl alcohol (99.5%) and acetone (99.5%) were purchased from Samchun Chemicals Co. Ltd. (Korea). All of the chemicals were used without further purification. Aqueous solutions were prepared with deionized (DI) water having a resistivity exceeding  $18.0 \text{ M}\Omega \text{ cm}^{-1}$ .

## 2.2. Synthesis of LaFeO<sub>3</sub> perovskite oxides

LFO microspheres were prepared *via* a hydrothermal process and post-calcination (**Figure 3**). Pluronic F127 (2 g) was dissolved in 50 mL of DI water. After that, La(NO<sub>3</sub>)<sub>3</sub>·6H<sub>2</sub>O (2.17 g, 5 mmol), Fe(NO<sub>3</sub>)<sub>3</sub>·9H<sub>2</sub>O (2.02 g, 5 mmol), and citric acid (1.92 g, 10 mmol) were added to the Pluronic F127 solution. The resulting solution was continuously agitated with magnetic stirrer for 4 h at 40 °C. The prepared precursor solution was poured into a Teflon-lined stainless steel autoclave and underwent a hydrothermal treatment at 180 °C for 12 h. After the autoclave was naturally cooled to room temperature, the product, red precipitations, was centrifuged and washed with DI water, ethyl alcohol, and acetone several times respectively, followed by drying in a vacuum oven at 60 °C overnight. The dried powders were ground finely by a mortar-pestle and subjected to calcination in air at 400–900 °C for 6 h with ramping temperature rate of 1 °C/min.

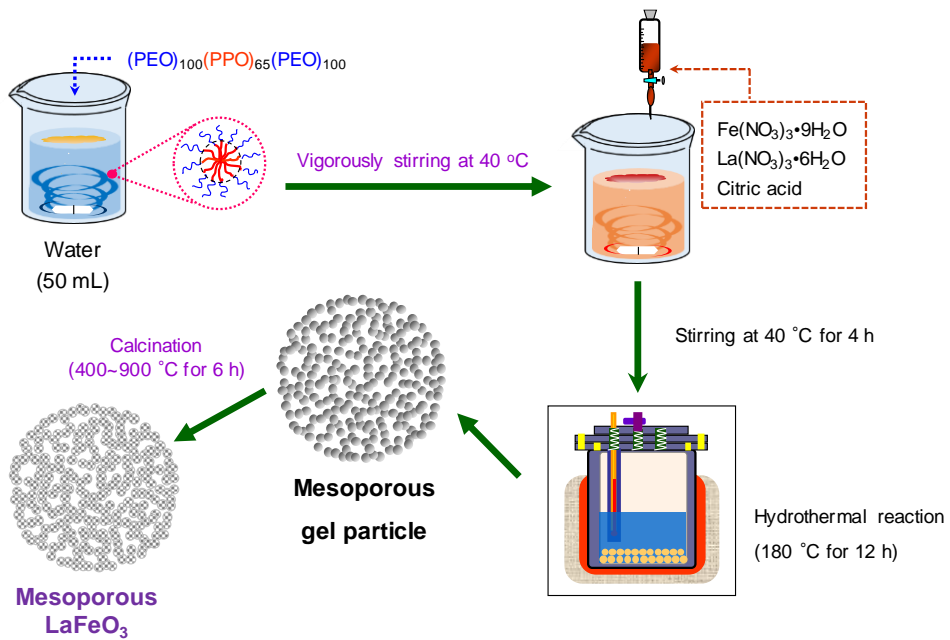


**Figure 3.** Schematic description of the synthetic procedure of  $\text{LaFeO}_3$  oxides

## 2.3. Synthesis of Ce-impregnated LaFeO<sub>3</sub> (CLFO series) catalysts

The synthesis of Ce-impregnated LaFeO<sub>3</sub> samples was described in **Figure 4**. LaFeO<sub>3</sub> perovskite oxide (1 g) was dispersed in a round-bottom flask filled with 20 mL of an Ce(NO<sub>3</sub>)<sub>3</sub>·6H<sub>2</sub>O aqueous solution. The calculated amount of cerium precursor was used based on the molar ratio compared to the total amounts of lanthanum cations. The solution with dispersed LaFeO<sub>3</sub> powder was stirred vigorously at room temperature for 3 h, followed by the vacuum evaporation of water and drying at 60 °C overnight. The dried powder was calcined at 800 °C for 2 h with a ramping rate of 1 °C/min, and was termed as CLFO-A. The alphabet A means after calcination.

CLFO-B (before calcination) was prepared by a similar method to CLFO-A. In this case, an amorphous LaFeO<sub>3</sub> precursor before calcination instead of calcined LaFeO<sub>3</sub> was used, and the other procedures were same to the above synthesis.

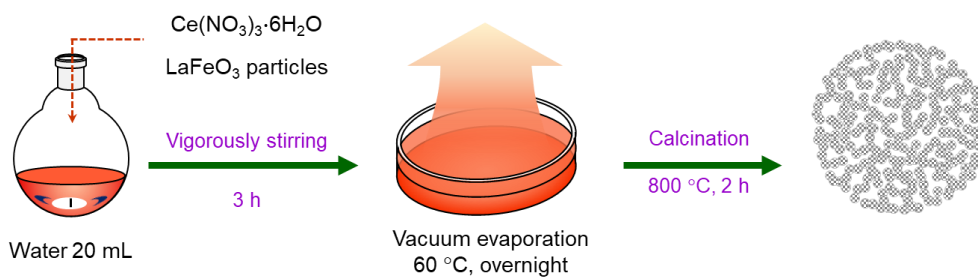


**Figure 4.** Schematic description of the synthetic procedure of CLFO series

## **2.4. Synthesis of Ce-substituted LaFeO<sub>3</sub> (LCFO series) catalysts**

The LCFO catalysts were prepared *via* a hydrothermal process and post-calcination similar to the synthesis of LaFeO<sub>3</sub> oxides. The calculated amount of Ce(NO<sub>3</sub>)<sub>3</sub>·6H<sub>2</sub>O was dissolved into the Pluronic F127 aqueous solution with other precursors. The molar ratio of the precursors was La : Ce : Fe : citric acid = 1-x : x : 1 : 2, where x is the calculated degree of substitution value. The other procedures were same except that temperatures of the hydrothermal treatment and calcination were fixed to 180 °C and 800 °C respectively.

## **2.5. Synthesis of yolk-shell structured LCFO catalysts**

The yolk-shell structured LCFO catalysts were synthesized with similar procedure of LCFO catalysts. To obtain the yolk-shell structure we controlled the ramping rates of the calcination temperature. Including 1 °C/min for the forementioned samples, the ramping rates were increased up to 10 °C/min and to investigate an extreme case we calcined amorphous LCFO in pre-heated furnace to 800 °C.

## 2.6. Catalyst characterization

The crystal structure of the catalysts was determined by powder X-ray diffraction (XRD) using a Bruker D8 Advance X-ray diffractometer with Cu-K $\alpha$  (50 kV, 100 mA,  $\lambda = 1.541 \text{ \AA}$ ) radiation. To characterize the surface chemical structures of catalysts X-ray photoelectron spectroscopy (XPS) was conducted by a Kratos AXIS-HSi spectrometer at a background pressure of about  $1.0 \times 10^{-9}$  Torr. The instrument for XPS was operated with a monochromatic Mg K $\alpha$  X-ray source at 10 mA. All binding energies were referenced to the C 1s peak at 285 eV, attributed to adventitious carbon.

The morphology of the catalysts was observed by field-emission scanning electron microscopy (FE-SEM) using a Carl Zeiss SUPRA 55VP microscope equipped with energy-dispersive spectroscopy (EDS) capabilities. Each samples were dried under vacuum and coated with platinum by a vacuum electric sputter prior to FE-SEM analysis. High-resolution transmission electron microscopy (HR-TEM, JEOL JEM-3010 microscope) was used to observe the shape and inner morphology of the catalysts. To prepare specimens samples were dispersed in ethyl alcohol by ultrasonic probe, placed on a carbon-coated copper grid and dried in vacuum.

The textural structures of catalysts were investigated by N<sub>2</sub> adsorption-desorption isotherms obtained at 77 K using a Micromeritics TriStar II 3020 analyzer. Prior to N<sub>2</sub> adsorption, the samples were degassed at 200 °C for 2 h. The specific surface areas (SSAs) were calculated by the Brunauer-Emmett-Teller (BET) model, and the distribution of pore size and the average pore size ( $D_{\text{avg}}$ ) was obtained from the Barrett-Joyner-Halenda (BJH) model.

The adsorbed sulfate species on the catalysts were monitored by Fourier transform infrared (FT-IR) spectroscopy using a Thermo Scientific Nicolet iS1. The catalysts were exposed to mixed gas including SO<sub>2</sub> for 1 h to investigate SO<sub>2</sub> adsorption behavior under SO<sub>2</sub> oxidation and NH<sub>3</sub>-SCR reaction condition, FT-IR analysis was conducted with pelletized samples with KBr over 500-4000 cm<sup>-1</sup> with a spectral resolution of 4 cm<sup>-1</sup>.

## 2.7. Catalyst performance tests

The catalytic activity tests were performed with a NH<sub>3</sub>-SCR reactor illustrated in **Figure 5**. The catalysts were located in a fixed bed tubular reactor having an internal diameter of 1 cm. The total gas flow rate was 1 L/min. The composition of the gas flow was [NO] = 400 ppm, [NH<sub>3</sub>] = 400 ppm, [O<sub>2</sub>] = 3 vol.% and [SO<sub>2</sub>] = 150 ppm (when used), and N<sub>2</sub> was used as the balance gas. The catalysts were loaded into the reactor, and the gas hourly space velocity (GHSV) adjusted to 20,000 h<sup>-1</sup>. The tests were conducted across a temperature range of 100–550 °C and the data were collected until the reaction reached a steady state. The concentrations of NO and NO<sub>2</sub> in the effluent gas were measured using a Testo 350K flue gas analyzer. NO conversion was calculated according to the following equation:

$$\text{NO conversion (\%)} = ([\text{NO}]_{\text{inlet}} - [\text{NO}]_{\text{outlet}}) / [\text{NO}]_{\text{inlet}} \times 100$$

where [NO]<sub>inlet</sub> indicates the inlet NO concentration; and [NO]<sub>outlet</sub> indicates the sum of the outlet NO and NO<sub>2</sub> concentrations.

SO<sub>2</sub> resistance was evaluated by detecting retention of the original NO conversion at 300 °C during continuous exposure to SO<sub>2</sub>-included mixed gas and after water regeneration process.

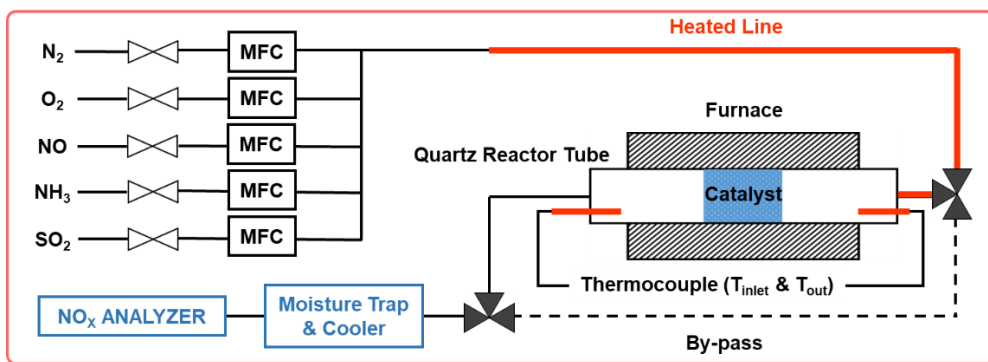


**Figure 5.** Schematic illustration of NH<sub>3</sub>-SCR reactor

## 3. Results and discussion

### 3.1. LaFeO<sub>3</sub> perovskite oxide microspheres

#### 3.1.1. Crystal structure

LaFeO<sub>3</sub> perovskite oxides were synthesized varying calcination temperature to investigate the effect of calcination process. The sample code was demonstrated as LFO 180-x, where x is temperature for calcination.

XRD analysis was conducted to determine the overall crystal structure of the prepared LFO samples (**Figure 6**). Above 600 °C of calcination temperature, crystalline structures appeared and the diffraction peaks at  $2\theta = 22.61, 32.20, 39.71, 46.17, 52.01, 57.41, 67.37, 72.06,$  and  $76.63^\circ$  well agreed with the LaFeO<sub>3</sub> perovskite oxide crystal structure (ICDD No. 01-070-7777).<sup>23</sup> In case of LFO 180-900, other diffraction peaks which are not related to perovskite structure were observed, indicating pure LaFeO<sub>3</sub> crystal phase was constructed until 800 °C of calcination.

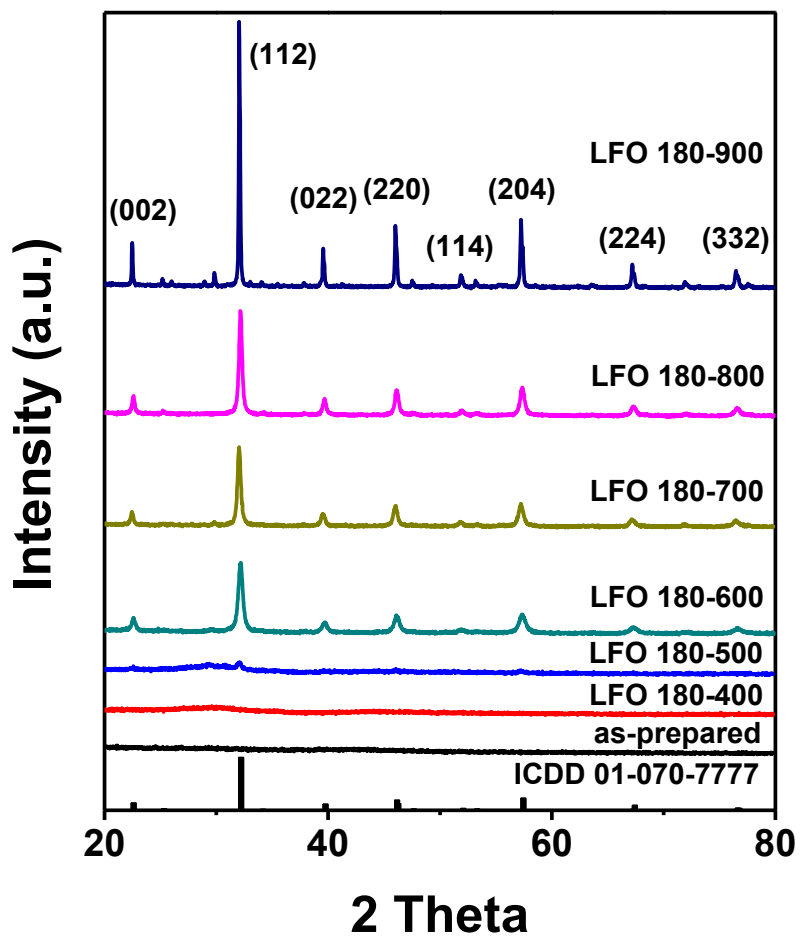
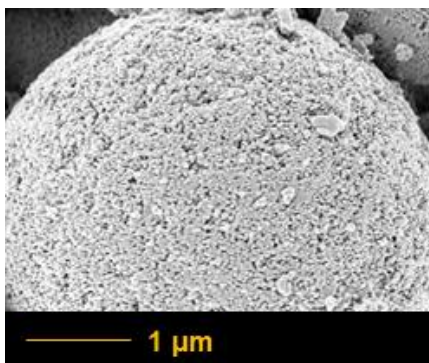


**Figure 6.** XRD patterns of LFO 180-x samples

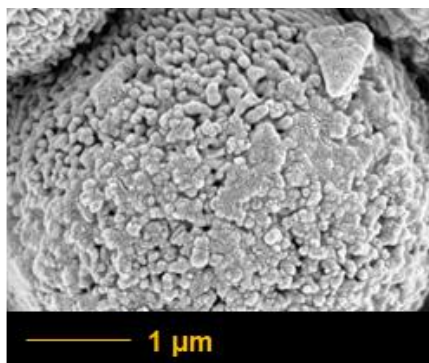
### 3.1.2. Morphological and textural structure

Morphology of the samples was observed by FE-SEM analysis as shown in **Figure 7**. All samples exhibited several micrometer-sized spherical shapes comprised of small primary particles regardless of temperature change. The formation of microspheres was attributed to the assembly of the primary particles by a shape-determination agent (a non-ionic surfactant, Pluronic F127). And the diameters of the primary particles became larger with increasing calcination temperature. Especially, this phenomenon occurred remarkably in LFO 180-800 and LFO 180-900 samples.

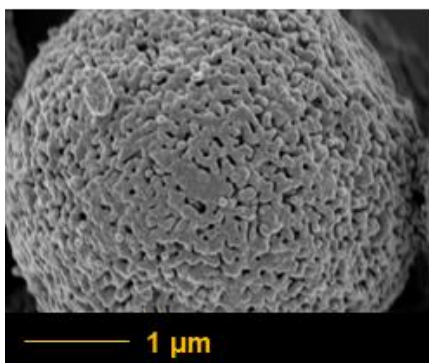
Textural properties of the catalysts were summarized in **Figure 8**. All samples exhibited average pore sizes in the range of 2-50 nm, indicating the synthesized oxides had the mesoporous structure. With increasing calcination temperature, specific surface area and pore volume were decreased. Average pore diameters were expanded from LFO 180-600 to LFO 180-700 samples and then shrank to LFO 180-900. Similar to the trend observed in FE-SEM images, the decreasing trends of pore diameters and pore volume were changed at around 800 °C. The pore diameters were reduced and the pore volume diminished significantly from LFO 180-800.



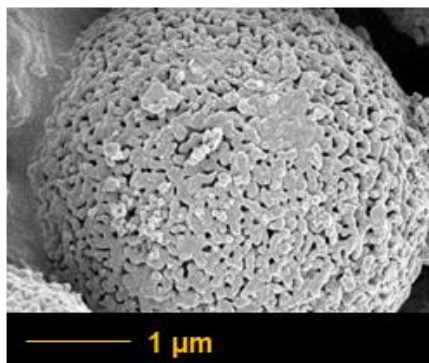
**LFO 180-600**



**LFO 180-700**



**LFO 180-800**



**LFO 180-900**

**Figure 7.** FE-SEM images of LFO 180-x samples

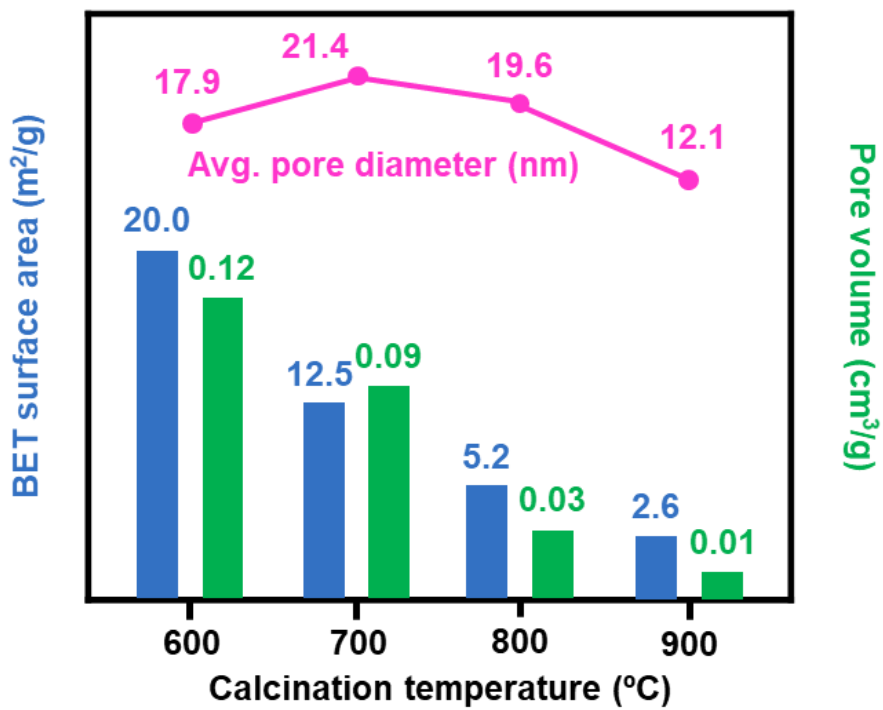


**Figure 8.** Textural properties of LFO 180-x samples

### 3.1.3. The effect of calcination temperature

**Figure 9** shows the relationship between calcination temperature and particle growth, which reflects the above results. Initially, particles grow based on surface diffusion under relatively low temperature. And then, boundary migration dominates beyond a certain temperature. In this system, the particle growth mechanism changed around 800 °C of calcination temperature. Leite group reported a similar trend with  $ZrTiO_3$  and  $NaNbO_3$  oxides.<sup>24</sup> They calculated average pore diameters of the oxides with different calcination temperatures. The resulting logarithm of diameter versus inverse temperature plot showed linear relationship and the slopes of two oxides changed based on 800 °C.

Crystallinity, morphology and textural properties are important factors to determine catalytic performance and durability. In this system, pure crystal structure was obtained until 800 °C of calcination, spherical morphology was constructed regardless of temperature change, and average pore diameter was significantly decreased in LFO 180-900. Considering the above mentioned results, LFO 180-800 sample was selected and named as LFO to further Ce-incorporation.

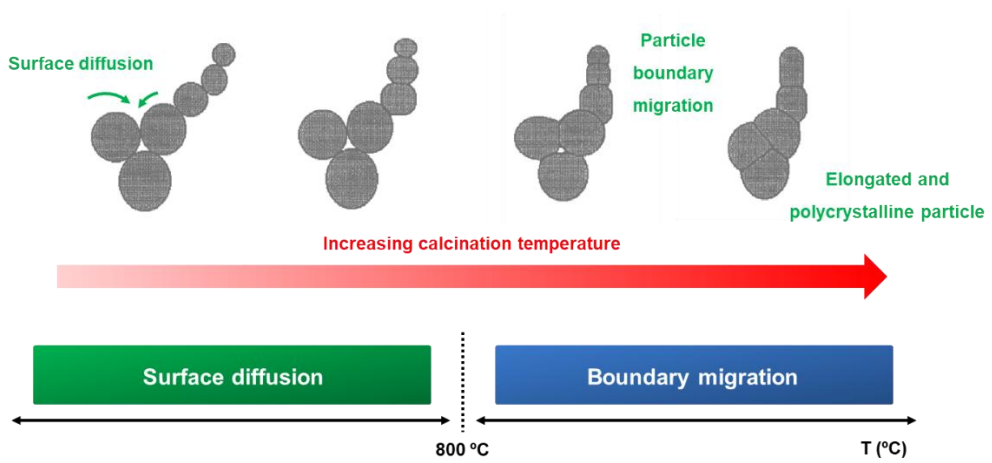


**Figure 9.** Mechanism of temperature-dependent particle growth

## 3.2. Ce-incorporated LaFeO<sub>3</sub> catalysts

### 3.2.1. Crystal structure

Cerium was incorporated into LFO differently to investigate more appropriate method for LaFeO<sub>3</sub> perovskite oxide. For this purpose, three samples i.e. LCFO, CLFO-A and CLFO-B were synthesized. **Figure 10** shows XRD results of the prepared LFO and the Ce-incorporated samples. All of four samples exhibited the diffraction peaks of LaFeO<sub>3</sub> perovskite oxide ( $2\theta = 22.61, 32.20, 39.71, 46.17, 52.01, 57.41, 67.37, 72.06, \text{ and } 76.63^\circ$ ). In the Ce-impregnated samples (CLFO-A and CLFO-B), a diffraction peak located at a  $2\theta$  value around  $29^\circ$  was observed, which is a characteristic peak of CeO<sub>2</sub> (ICDD No. 00-034-0394).<sup>25</sup> And CLFO-B showed a relatively strong ceria peak and weak perovskite peaks compared to CLFO-A, which was attributed to inhibition of crystallization of the perovskite oxide due to the deposited Ce ions and co-crystallization of ceria with citric acid-chelated metal cations on surface of precursor particles. On the other hand, LCFO exhibited a pure perovskite phase. Especially, the slight shift of the diffraction peaks to higher  $2\theta$  angles indicated the Ce ions successfully substituted the La position. The ionic radii of Ce were similar to La but slightly large (La<sup>3+</sup>, 150 pm; Ce<sup>3+</sup>, 148 pm; Ce<sup>4+</sup>, 128 pm).<sup>16</sup>

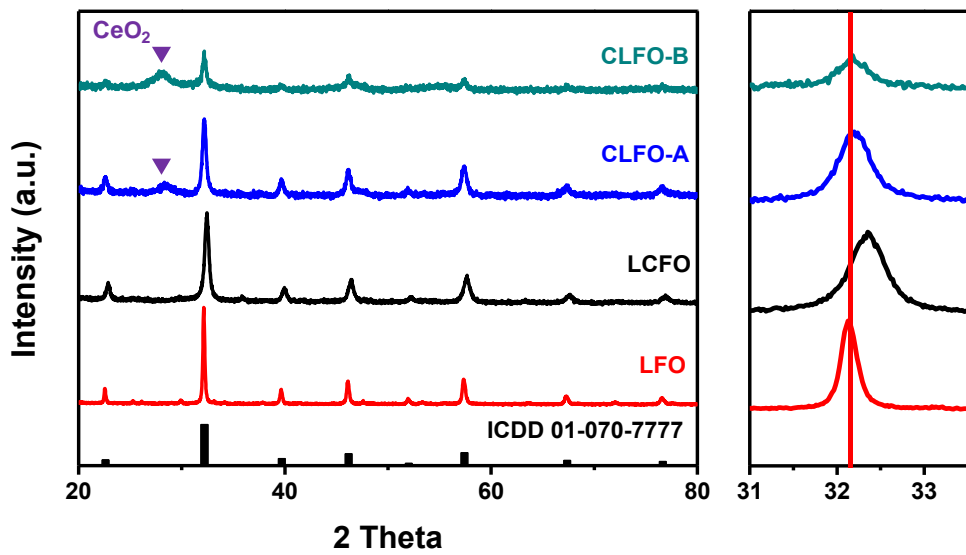


**Figure 10.** XRD patterns of LFO and Ce-incorporated samples

### 3.2.2. Morphological and textural structure

FE-SEM and HR-TEM were utilized to observe morphology of the samples. As shown in **Figure 11**, all of four samples exhibited spherical shape with a few micrometers of diameter which is the morphology of LFO. Micrographs of LCFO were very similar to LFO results, microspheres without other particles. It meant LCFO did not include other compounds, which was consistent with XRD results. In comparison, the FE-SEM micrographs of CLFO-A and CLFO-B displayed additional particles on the surface of the perovskite microspheres. Considering XRD patterns of the samples, it is suggested that these small particles are cerium oxide. In addition, larger-sized particles were observed on CLFO-B sample because crystallization of cerium oxides during calcination step metal cations on surface of the amorphous  $\text{LaFeO}_3$  precursor participated in constructing crystal structure. This is supported by the enhanced ceria peak and weakened perovskite peaks in the XRD patterns of CLFO-B.

Textural properties of the samples were investigated by  $\text{N}_2$  adsorption/desorption.  $\text{N}_2$  sorption isotherms were illustrated in **Figure 12**. All samples displayed type-IV isotherms and H1-type hysteresis loops which were the characteristics of mesoporous structures. BJH pore-size distribution in **Figure 13** indicated the samples exhibited a broad range of pore sizes.

Numerical data were summarized in **Table 1**. The specific surface area (SSA) calculated by the BET method. SSA value of LCFO was similar to LFO, while SSA increases for CLFO-A and CLFO-B. Perovskite oxides are typically comprised by large primary particles because of high temperature calcination procedure, resulting in low SSA values.<sup>26</sup> In this system, the deposited ceria having a smaller crystallite size is thought to make CLFO-A and CLFO-B possess higher SSA and pore volumes.

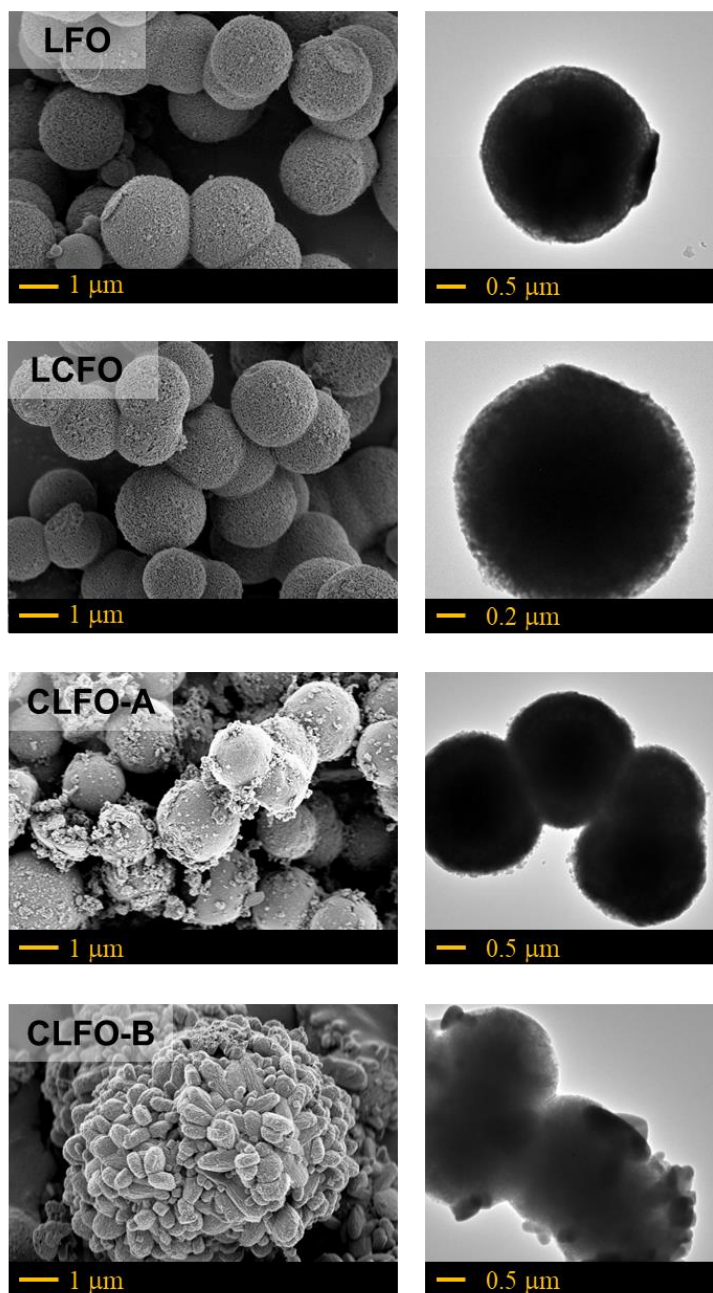


**Figure 11.** FE-SEM and HR-TEM images of the samples

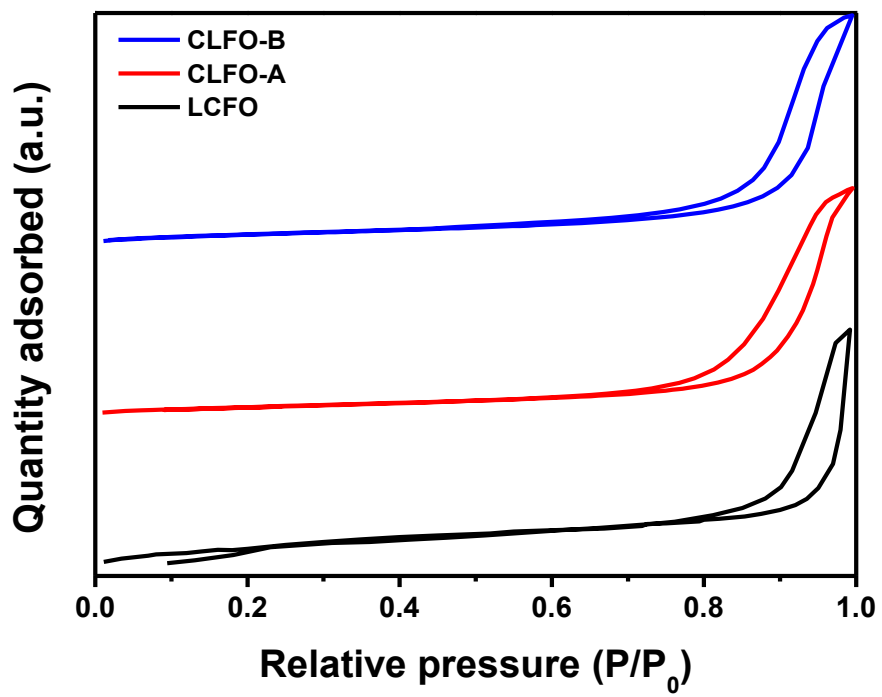
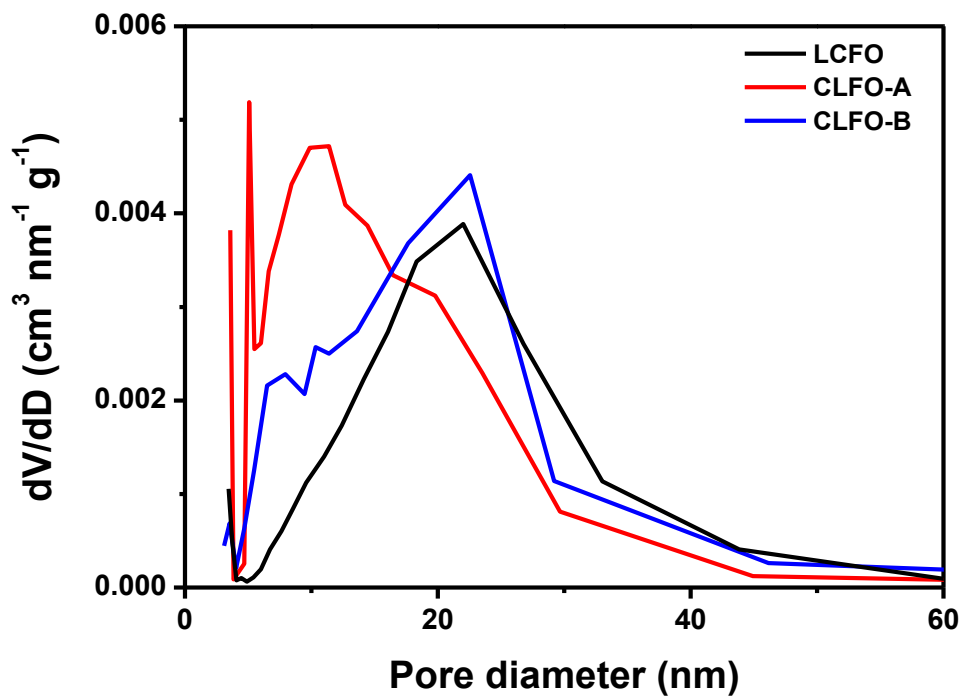


Figure 12. N<sub>2</sub> sorption isotherms of the samples



**Figure 13.** BJH pore-size distribution of the samples

**Table 1.** Summary of N<sub>2</sub> adsorption/desorption analysis

<b>Sample</b>	<b>Specific surface area (m<sup>2</sup>/g)</b>	<b>Average pore diameter (nm)</b>	<b>Pore volume (cm<sup>3</sup>/g)</b>
LCFO	4.5	22.6	0.029
CLFO-A	12.7	14.5	0.078
CLFO-B	19.1	20.2	0.120

### 3.2.3. Surface chemical structure

The atomic composition and chemical state on the surface of the catalysts were studied by XPS. La 3d and Fe 2p spectra of the samples indicated that the structures were principally constructed by cations of III–III valence states (not shown here). The La 3d core-level spectra of the samples shows two major peaks at ~833 and ~850 eV, attributed to the 3d<sub>5/2</sub> and 3d<sub>3/2</sub> spin-orbit peaks of La<sup>3+</sup> ions.<sup>27</sup> The Fe 2p spectra of the catalysts also displayed two major peaks associated with the 2p<sub>3/2</sub> and 2p<sub>1/2</sub> states of Fe ions. The spin-orbit peaks of the 2p<sub>3/2</sub> state are observed at ~710 eV, which suggests that the Fe ions mainly comprise Fe<sup>3+</sup> valence states in the perovskite structure.<sup>28</sup>

The Ce 3d core-level XPS spectra were shown in **Figure 14** and deconvoluted into eight peaks attributed to the Ce<sup>3+</sup>/Ce<sup>4+</sup> mixed valence states of cerium ions. Among those peaks, v (centered at 882.29 eV), v'' (888.73 eV), v''' (898.09 eV), u (900.67 eV), u'' (907.67 eV) and u''' (916.68 eV) are ascribed to Ce<sup>4+</sup> species, and v' (884.79 eV) and u' (903.29 eV) are attributed to Ce<sup>3+</sup> species.<sup>29</sup> The calculated Ce<sup>3+</sup> ratio values, on a total cerium ion basis, are also listed in **Table 2**. Among the Ce-incorporated samples, LCFO possess more Ce<sup>3+</sup> species compared with the other catalysts. It is generally accepted that Ce<sup>3+</sup> is related to the formation of oxygen vacancies or surface chemisorbed

oxygen species and appropriate ratio of  $\text{Ce}^{3+}$  species facilitates  $\text{Ce}^{3+}/\text{Ce}^{4+}$  redox cycles.<sup>30</sup>

The O 1s spectra presented one broad peak, which can be deconvoluted into two peaks with binding energies at 528.7 and 530.8 eV (**Figure 15**). The lower energy peak was ascribed to the lattice oxygen (metal–oxygen) species, and the higher energy peak is attributed to the surface chemisorbed oxygen  $\text{O}^-$  or  $\text{OH}^-$  species.<sup>31</sup> A 2.1–2.5 eV shift to higher binding energies is typically reported for the latter peak.<sup>32</sup> The calculated ratio of surface oxygen ( $\text{O}_s$ ) to lattice oxygen ( $\text{O}_L$ ) is observed to be the highest in LCFO (**Table 2**). The  $\text{O}_s$  ratio is usually related to the oxygen vacancy density and the surface-active oxygen species, which suggests a higher number of such species on the surface of LCFO. Therefore, substituted cerium cations enhanced  $\text{Ce}^{3+}$  and  $\text{O}_s$  ratio of the  $\text{LaFeO}_3$  perovskite oxide compared to impregnated Ce elements and the substituted sample, LCFO, was expected to exhibit an improved catalytic performance.

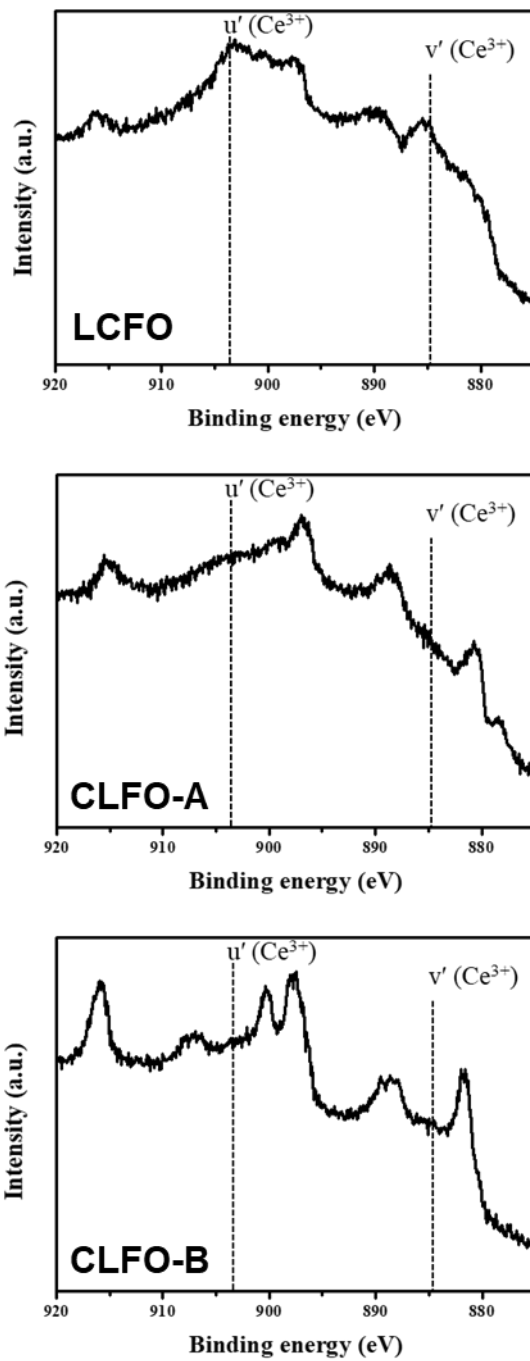


**Figure 14.** Ce 3d core-level XPS spectra of the samples

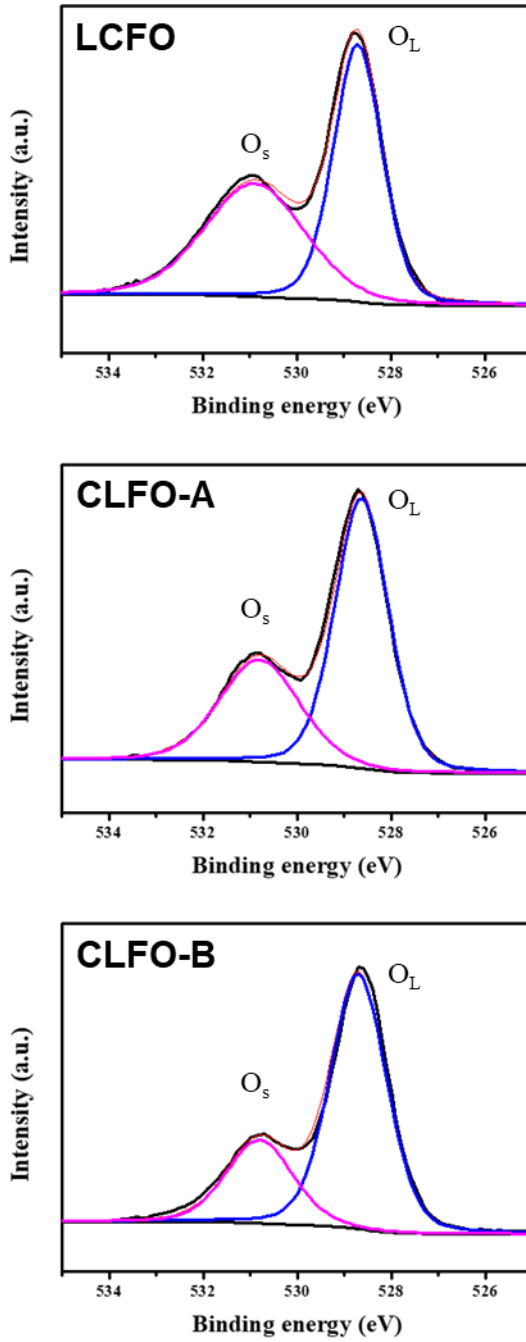


**Figure 15.** O 1s core-level XPS spectra of the samples

**Table 2.** Surface atomic ratio of Ce/La,  $O_S/(O_S+O_L)$  and  $Ce^{3+}/(Ce^{3+}+Ce^{4+})$  calculated from XPS results of the samples

<b>Sample</b>	<b>Ce/La (%)</b>	<b><math>O_S/(O_S + O_L)</math> (%)</b>	<b><math>Ce^{3+}/(Ce^{3+} + Ce^{4+})</math> (%)</b>
LCFO	10.2	47.3	26.2
CLFO-A	9.3	35.8	16.6
CLFO-B	10.6	27.8	12.2

### 3.2.4. NH<sub>3</sub>-SCR performance

The SCR performances of the LFO and Ce-incorporated perovskite oxides are shown in **Figure 16**. The LFO microspheres exhibit poor NO conversion across the entire temperature range studied, and shows a broad peak centered at 300 °C with a conversion ratio of ca. 10%. Zhang *et al.* studied several perovskite-type catalysts for NH<sub>3</sub>-SCR, including LaFeO<sub>3</sub> catalyst.<sup>12</sup> Compared to the LFO catalyst herein, their results also presented a similar shaped curve.

NO conversion curves of CLFO-A and CLFO-B, Ce-impregnated samples, had similar shapes but their efficiencies were enhanced up to 40% at 300 °C. The reaction temperatures where the highest NO conversion occurred were slightly different but there was no significant difference between the two samples. The improvement of catalytic activities of the Ce-impregnated catalysts would be contributed to ability of the deposited ceria to adsorb and deliver NH<sub>3</sub> to main active sites of perovskite oxides. One of the major problems of poor NH<sub>3</sub>-SCR performance on LaFeO<sub>3</sub> catalyst is a low adsorptive ability of ammonia.<sup>12</sup> The impregnated ceria helped to catch the gaseous NH<sub>3</sub> and facilitate SCR reaction on LaFeO<sub>3</sub> catalysts (**Figure 17**).<sup>33</sup> However, this effect on improvement was not strong enough because the original efficiency of LFO in SCR was poor.

The NO conversion curve of LCFO showed high catalytic performance across a wide temperature window compared to the other samples. The highest efficiency was ca. 70% at 300 °C of operation temperature. And decrease in NO conversion is observed at reaction temperatures above 450 °C as a result of the accumulation of inert ionic nitrates on the surface. It has been reported that SCR activity for NO gradually decreases in the presence of inert ionic species, *e.g.* Fe(NO<sub>3</sub>)<sub>3</sub>, when the reaction temperature increases to 400 °C.<sup>34</sup> The XRD results indicated that all of the incorporated Ce ions substituted La sites in the LFO crystal structure. This structural modification directly formed a new active site, Ce–O–Fe, resulting in the enhanced the concentration of O<sub>s</sub> and Ce<sup>3+</sup> species.<sup>35-37</sup> Especially, metal cations need to be oxidized in SCR system because they are reduced after reaction as shown in **Figure 18**. This oxidation step is so slow that the entire reaction rate is determined by this step in most of NH<sub>3</sub>-SCR systems.<sup>38</sup> The substituted cerium cations could facilitate the oxidation step of Fe cations, the active sites of LaFeO<sub>3</sub> perovskite oxides, utilizing their Ce<sup>3+</sup>/Ce<sup>4+</sup> redox cycle.

Even though the SCR performance of LaFeO<sub>3</sub> was significantly enhanced by Ce-incorporation, there was still room for improvement by morphological control. LCFO with the highest NO conversion was selected to further improvement by introducing yolk-shell structure.

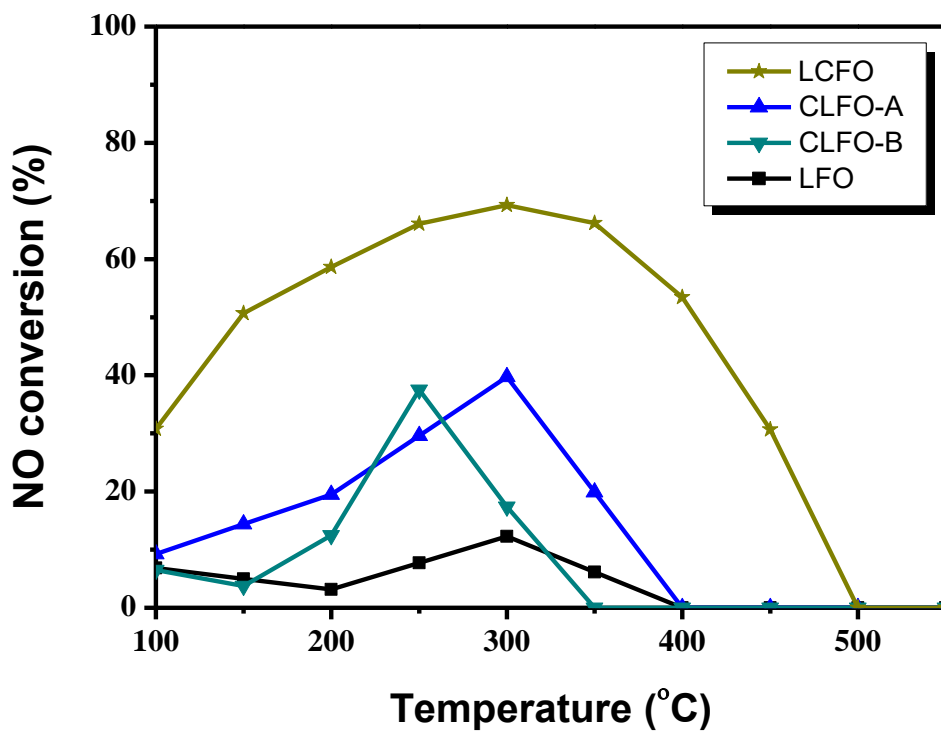


**Figure 16.** NH<sub>3</sub>-SCR performance of the catalysts

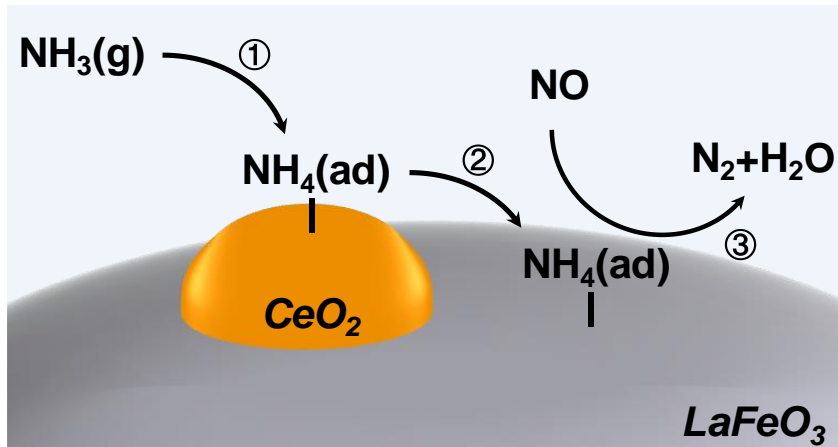


**Figure 17.** Proposed role of impregnated ceria in  $\text{NH}_3$ -SCR reaction

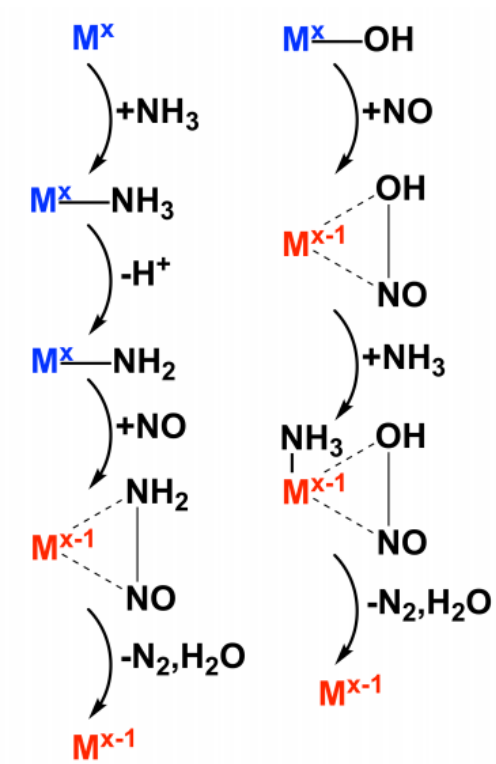


**Figure 18.** General mechanism of  $\text{NH}_3$ -SCR reaction

### 3.3. Yolk-shell structured LCFO

#### 3.3.1. Morphological structure

Further enhancement of LCFO by introduction of the yolk-shell structure was achieved through changing a simple experimental variable, ramping rate of calcination temperature. The initial ramping rate of 1 °C/min was raised to 10 °C/min.

FE-SEM and HR-TEM images of LFO and LCFO with different ramping rates are listed in **Figure 19**. In the images of LCFO with ramping rate of 10 °C/min, yolk-shell structured particles with the movable core@void@outer shell configuration were observed. The formation of yolk-shell structure by varying calcination condition was explained by heterogeneous contraction illustrated in **Figure 20**.<sup>21,22</sup> With fast ramping rate, difference of thermal energy transfers between inside and outside of particle occurs and various type of structures are generated depending on ramping rate of temperature. For yLCFO, the yolk-shell structured was achieved by high rate of temperature ramping during calcination. In case of LFO, however, 10 °C/min of ramping rate did not induce the yolk-shell structure. To investigate the extreme condition, LFO precursor was put in a furnace pre-

heated to 800 °C but yolk-shell structure did not take place (not shown). Basically ramping rate is the most important factor determining product morphology, but other factors such as composition and precursor size etc. also affect this phenomenon. Cerium substitution in LCFO affected significantly to catalytic properties and also attributed to construction of yolk-shell structure. Yolk-shell structure was observed when LCFO precursor underwent calcination pre-heated to 800 °C, and additional morphological change was not detected. Therefore,  $\gamma$ LCFO with the ramping rate of 10 °C/min was selected for evaluation of NH<sub>3</sub>-SCR performance.

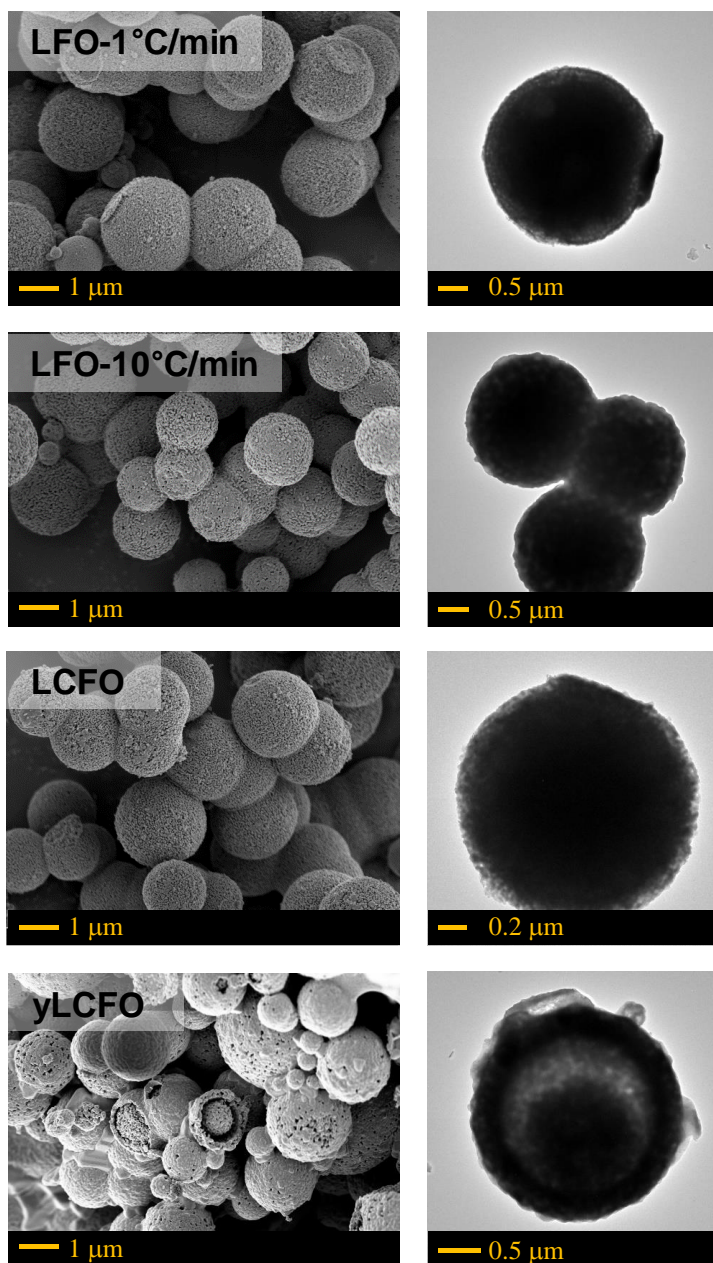


**Figure 19.** FE-SEM and HR-TEM images of the samples



### 3.3.2. NH<sub>3</sub>-SCR performance

The SCR performance of yLCFO compared with LFO and LCFO is shown in **Figure 21**. The NO conversion efficiency of LCFO was further increased and the catalyst exhibited the highest efficiency value ca. 90% at 300–450 °C. In addition to the highest value, operating temperature window was significantly expanded. The textural properties of LCFO were not changed notably in spite of introducing yolk-shell structure. It might be because initial properties of perovskite oxides were not good enough. In case of LCFO, SSA and pore volume were worse than other samples. Therefore, the enhancement of yLCFO was apparently contributed to construction of yolk-shell structure. There are numerous studies relating the effect of yolk-shell morphologies to catalytic performance. The yolk-shell structure can be considered as a suitable reactor to provide a reactant-rich microenvironment resulting in more effective reaction (**Figure 22**).<sup>39-41</sup> Based on the superior properties, LCFO was selected to undergo further SO<sub>2</sub> resistance and stability tests.

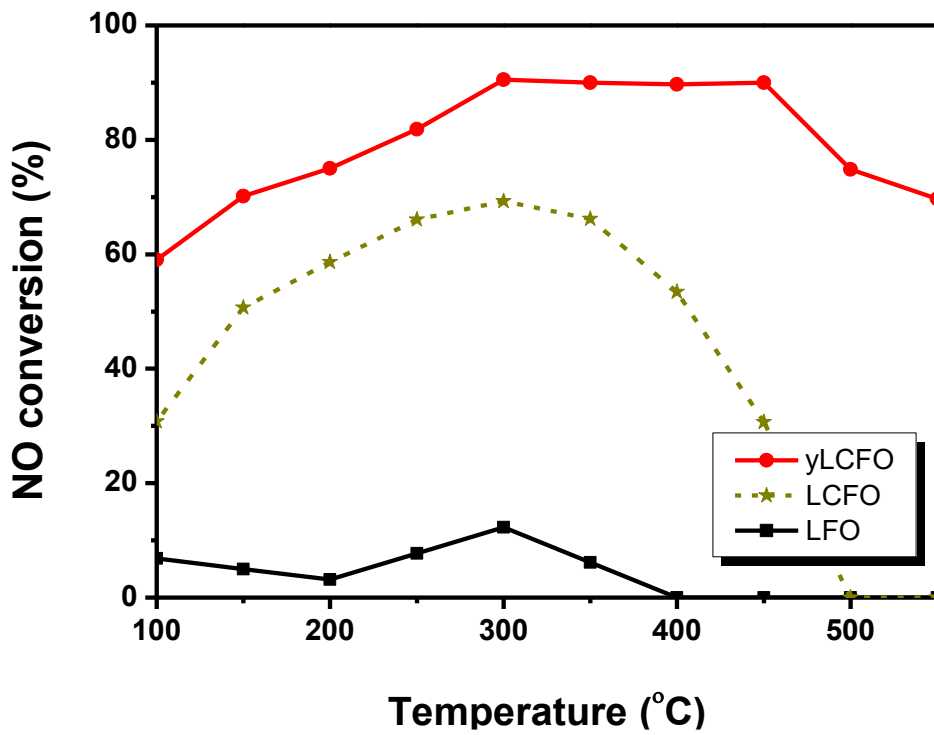


**Figure 21.** NH<sub>3</sub>-SCR performance of the samples

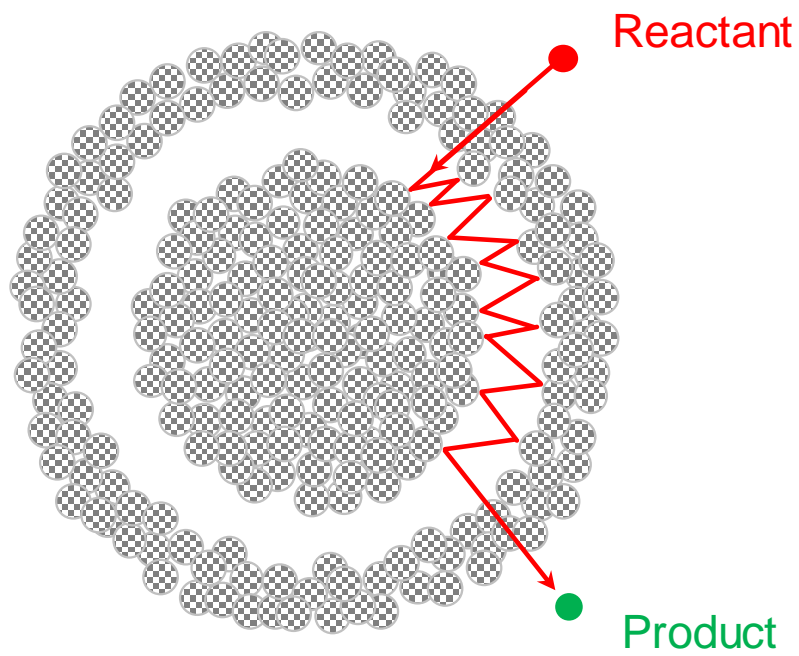


**Figure 22.** Plausible mechanism of the enhanced catalytic activity  
by introducing yolk-shell structure

### 3.3.3. SO<sub>2</sub> resistance

Before evaluation of SO<sub>2</sub> resistance of yLCFO, FT-IR analysis was conducted to investigate adsorption properties of gaseous reactants. **Figure 23** shows adsorption under oxidative condition of SO<sub>2</sub> (SO<sub>2</sub> + O<sub>2</sub>) on the catalysts. FT-IR peaks were observed in three areas contributed to LaFeO<sub>3</sub> oxides (I), weakly adsorbed sulfates species (II) and strongly adsorbed sulfate species (III).<sup>42,43</sup> After exposure to SO<sub>2</sub>, peaks ascribed to weakly adsorbed sulfates were observed on both LFO and yLCFO. However, strongly adsorbed species were not detected on yLCFO in spite of SO<sub>2</sub> exposure, which means sulfur resistance of yLCFO was higher than LFO.

**Figure 24** is FT-IR results of the samples after exposure to NH<sub>3</sub>-SCR condition with SO<sub>2</sub> at 300 °C. In this case, absorption peaks of adsorbed ammonia appeared in III area.<sup>44,45</sup> This ammonia peak was detected on both LFO and yLCFO surfaces. However, the peaks in II area related to sulfate species was very weakly detected in yLCFO. Therefore, it can be seen that SO<sub>2</sub> in mixed gas was not dominant to other reactant gases on yLCFO. This SO<sub>2</sub> resistance of yLCFO was confirmed by following performance test.

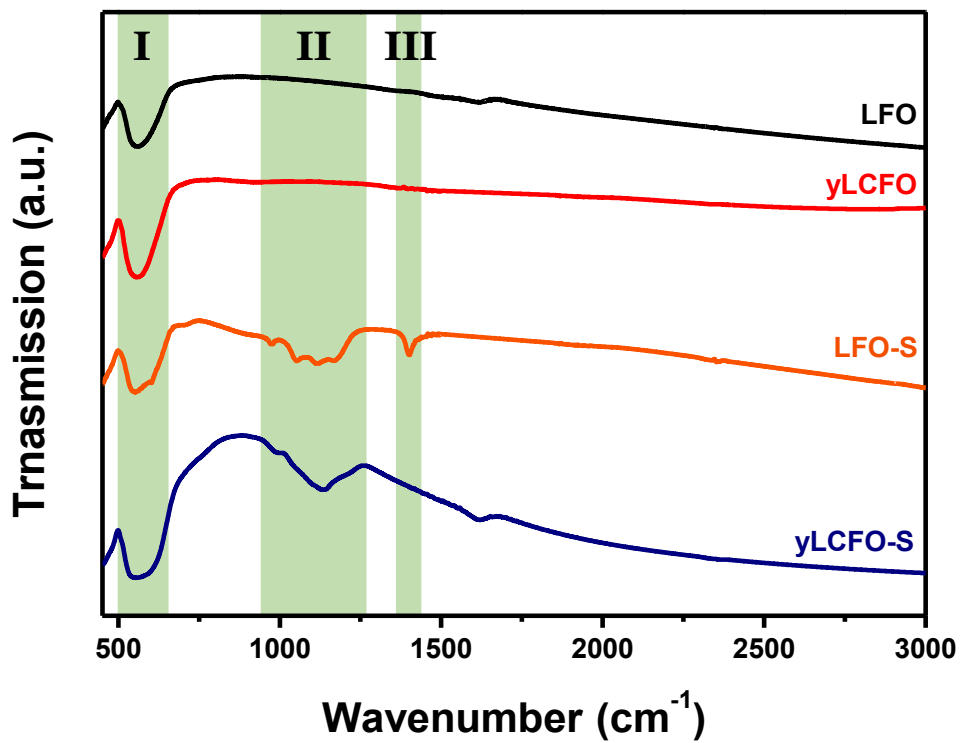


**Figure 23.** FT-IR results of the samples after  $\text{SO}_2 + \text{O}_2$  exposure

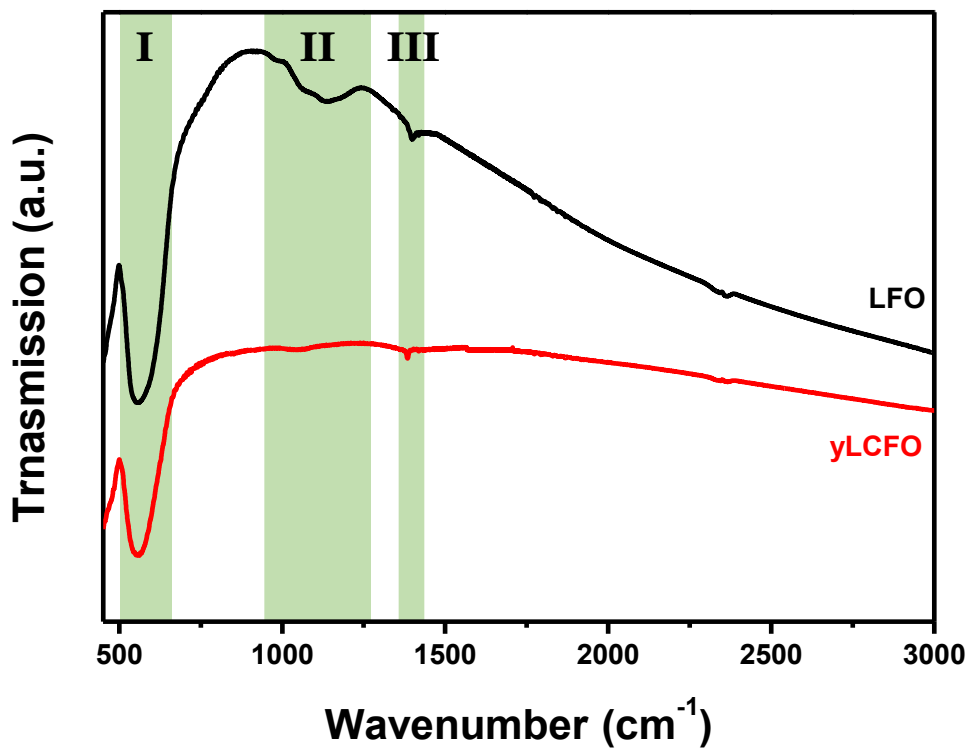
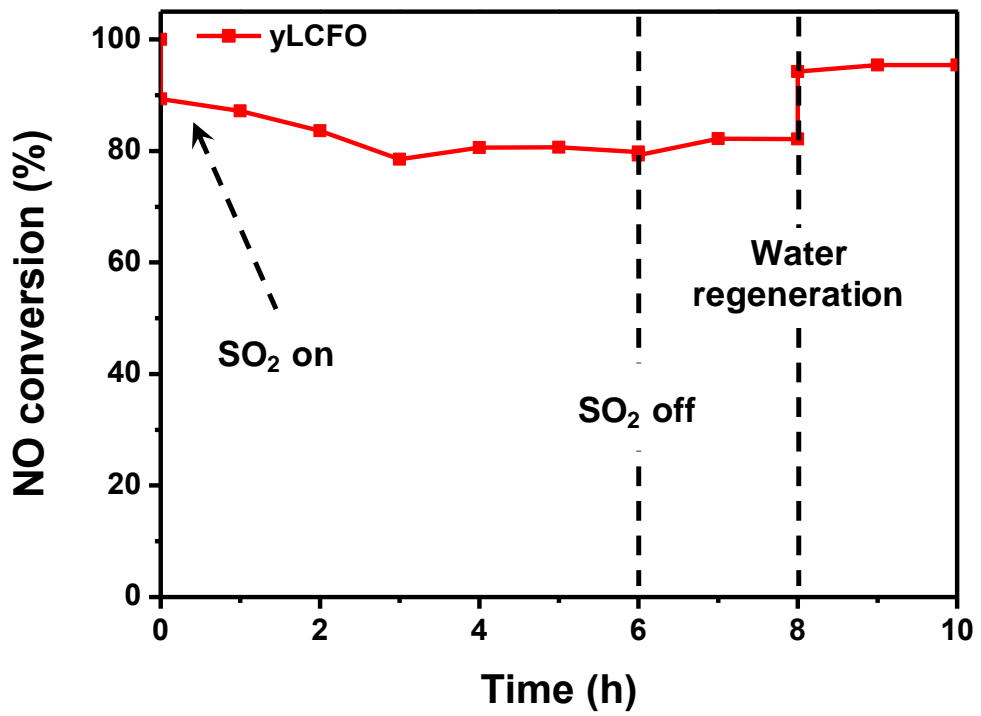


Figure 24. FT-IR results of the samples after  $\text{NH}_3$ -SCR reaction with  $\text{SO}_2$

**Figure 25** describes the SO<sub>2</sub> resistance test of  $\gamma$ LCFO under NH<sub>3</sub>-SCR conditions. When 150 ppm of SO<sub>2</sub> was injected into the input flue gas, NO conversion instantly decreased to around 90% and gradually further decreased to 80%, and the conversion efficiency was maintained until the SO<sub>2</sub> gas was eliminated from inlet gas. After a simple water regeneration process (just washed by DI water and dried), almost of the SCR catalytic activity was recovered, indicating the high SO<sub>2</sub> tolerance of LCFO and that deactivation by sulfur is recoverable. The SO<sub>2</sub> resistant properties of LCFO is suggested to originate from the reactivity and redox properties of the Ce species. Substituted Ce<sup>4+</sup> ions on the surface of the perovskite oxide displayed an ability to absorb, and release SO<sub>2</sub> on the surface of catalysts, protecting the active sites from sulfur poisoning.<sup>46</sup> The washable sulfur compounds indicated SO<sub>2</sub> was weakly adsorbed and did not generate a stable Fe-chelated species. There would exist an equilibrium between the adsorption and desorption of sulfur compounds during NH<sub>3</sub>-SCR reaction. SO<sub>2</sub> has been reported to competitively adsorb on the surface of catalyst with nitric oxide.<sup>47</sup>



**Figure 25.** SO<sub>2</sub> resistance test and water regeneration of yLCFO

## 4. Conclusion

In this research, we developed Ce-incorporated and yolk-shell structured  $\text{LaFeO}_3$  perovskite oxides *via* a hydrothermal treatment and heterogeneous contraction during calcination. Ce-incorporated  $\text{LaFeO}_3$  catalysts were synthesized by various methods to investigate appropriate way for perovskite oxides utilizing as  $\text{NH}_3$ -SCR catalysts. The differences between incorporated samples studied through characterization by XRD, FE-SEM, HR-TEM,  $\text{N}_2$  sorption and XPS. Depending on how the Ce precursor is added, LCFO exhibited a pure perovskite structure by the substitution of La ions with Ce ions. Conversely, the CLFO series were comprised a ceria-LFO composite structure. Substituted LCFO sample showed the highest  $\text{NH}_3$ -SCR performance among cerium-incorporated catalysts, which was contributed to the high concentration of  $\text{O}_s$  and the  $\text{Ce}^{3+}$  species of LCFO by Ce-substitution. To further improvement of LCFO, yolk-shell structure was induced by control of ramping temperature rate during calcination. And Ce ion substitution was demonstrated to influence the morphology, chemical state and catalytic performance of  $\text{LaFeO}_3$ . The yLCFO showed remarkable NO conversion efficiency (ca. 9 times higher than pristine  $\text{LaFeO}_3$ ) and  $\text{SO}_2$  tolerance. This work provides a way to utilize perovskite oxide-based catalysts for  $\text{NH}_3$ -SCR.

## References

- [1] Bacariza M. C.; Mendes A. N.; Ozhan, C.; Costa, P. D.; Henriques, C., Optimizing washcoating conditions for the preparation of zeolite-based cordierite monoliths for  $\text{NO}_x/\text{CH}_4$ -SCR: a required step for real application. *Industrial & Engineering Chemistry Research* **2019**, *58* (27), 11799–11810.
- [2] Roy, S.; Hegde, M. S.; Madras, G., Catalysis for  $\text{NO}_x$  abatement. *Applied Energy* **2009**, *86* (11), 2283–2297.
- [3] Granger, P.; Parvulescu, V. I., Catalytic  $\text{NO}_x$  abatement systems for mobile sources: from three-way to lean burn after-treatment technologies. *Chemical Review* **2011**, *111*, 3155–3207.
- [4] Boningari, T.; Smirniotis, P. G., Impact of nitrogen oxides on the environment and human health: Mn-based materials for the  $\text{NO}_x$  abatement. *Current Opinion in Chemical Engineering* **2016**, *13*, 133–141.
- [5] Fu, M.; Li, C.; Lu, P.; Qu, L.; Zhang, M.; Zhou, Y.; Yu, M.; Fang, Y., A review on selective catalytic reduction of  $\text{NO}_x$  by supported catalysts at 100–300 °C—catalysts, mechanism, kinetics. *Catalysis Science & Technology* **2014**, *4*, 14–25.
- [6] Nova, I.; Lietti, L.; Tronconi, E.; Forzatti, P., Dynamics of SCR

- reaction over a TiO<sub>2</sub>-supported vanadia-tungsta commercial catalyst. *Catalysis Today* **2000**, *60*, 73–82.
- [7] Liu, F.; Shan, W.; Shi, X.; He, H., Vanadium-based catalysts for the selective catalytic reduction of NO<sub>x</sub> with NH<sub>3</sub> *Progress in Chemistry* **2012**, *24*, 445–455.
- [8] Gao, F.; Tang, X.; Yi, H.; Zhao, S.; Li, C.; Li, J.; Shi, Y.; Meng, X., A review on selective catalytic reduction of NO<sub>x</sub> by NH<sub>3</sub> over Mn-based catalysts at low temperatures: catalysts, mechanisms, kinetics and DFT calculations. *Catalysts* **2017**, *7*, 199–230.
- [9] Royer, S.; Duprez, D.; Can, F.; Courtois, X.; Batiot–Dupeyrat, C.; Laassiri, S.; Alamdari, H., Perovskites as substitutes of noble metals for heterogeneous catalysis: dream or reality. *Chemical Review* **2014**, *114* (20), 10292–10368.
- [10] Zhu, J.; Li, H.; Zhong, L.; Xiao, P.; Xu, X.; Yang, X.; Zhao, Z.; Li, J., Perovskite oxides: preparation, characterizations, and applications in heterogeneous catalysis. *ACS Catalysis* **2014**, *4* (9), 2917–2940.
- [11] Zhu, H.; Zhang, P.; Dai, S., Recent advances of lanthanum–based perovskite oxides for catalysis. *ACS Catalysis* **2015**, *5* (11), 6370–6385.
- [12] Zhang, R.; Luo, N.; Yang, W.; Liu, N.; Chen, B., Low–temperature selective catalytic reduction of NO with NH<sub>3</sub> using perovskite–type

- oxides as the novel catalysts. *Journal of Molecular Catalysis A: Chemical* **2013**, *371*, 86–93.
- [13] Zhang, R.; Yang, W.; Luo, N.; Li, P.; Lei, Z.; Chen, B., Low-temperature NH<sub>3</sub>-SCR of NO by lanthanum manganite perovskites: effect of A-/B-site substitution and TiO<sub>2</sub>/CeO<sub>2</sub> support. *Applied Catalysis B: Environmental* **2014**, *146*, 94–104.
- [14] Shen, Y.; Ma, Y.; Zhu, S., Promotional effect of zirconium additives on Ti<sub>0.8</sub>Ce<sub>0.2</sub>O<sub>2</sub> for selective catalytic reduction of NO. *Catalysis Science & Technology* **2012**, *2* (3), 259–299.
- [15] Ma, Z.; Wu, X.; Si, Z.; Wenga, D.; Ma, J.; Xu, T., Impacts of niobia loading on active sites and surface acidity in NbO<sub>x</sub>/CeO<sub>2</sub>-ZrO<sub>2</sub> NH<sub>3</sub>-SCR catalysts. *Applied Catalysis B: Environmental* **2015**, *179*, 380–394.
- [16] Lay, E.; Benamira, M.; Pirovano, C.; Gauthier, G. H.; Dessemond, L., Effect of Ce-doping on the electrical and electrocatalytical behavior of La/Sr chromo-manganite perovskite as new SOFC anode. *Fuel Cells* **2012**, *12* (2), 265–274.
- [17] Li, Z.; Mo, L.; Kathiraser, Y.; Kawi, S., Yolk-satellite-shell structured Ni-yolk@Ni@SiO<sub>2</sub> nanocomposite: superb catalyst toward methane CO<sub>2</sub> reforming reaction. *ACS Catalysis* **2014**, *4* (5), 1526–1536.

- [18] Bie, S.; Zhu, Y.; Su, J.; Jin, C.; Liu, S.; Yang, R.; Wu, J., One-pot fabrication of yolk-shell structured  $\text{La}_{0.9}\text{Sr}_{0.1}\text{CoO}_3$  perovskite microspheres with enhanced catalytic activities for oxygen reduction and evolution reactions. *Journal of Materials Chemistry A* **2015**, *3* (44), 22448–22453.
- [19] Zhao, Q.; Wu, C.; Cong, L.; Zhang, Y.; Sun, G.; Xie, H.; Sun, L.; Liu, J., Yolk-shell  $\text{Co}_2\text{CrO}_4$  nanospheres as highly active catalysts for Li- $\text{O}_2$  batteries: understanding the electrocatalytic mechanism. *Journal of Materials Chemistry A* **2017**, *5* (2), 544–553.
- [20] Cho, E. C.; Camargo, P. H. C.; Xia, Y., Synthesis and characterization of noble-metal nanostructures containing gold nanorods in the center. *Advanced Materials* **2010**, *22* (6), 744–748.
- [21] Guan, J.; Mou, F.; Sun, Z.; Shi, W., Preparation of hollow spheres with controllable interior structures by heterogeneous contraction. *Chemical Communications* **2010**, *46* (35), 6605–6607.
- [22] Hong, Y. J.; Son, M. Y.; Park, B. K.; Kang, Y. C., One-pot synthesis of yolk-shell materials with single, binary, ternary, quaternary, and quinary systems. *Small* **2013**, *9* (13), 2224–2227.
- [23] Celorrio, V.; Bradley, K.; Weber, O. J.; Hall, S. R.; Fermín, D. J., Photoelectrochemical properties of  $\text{LaFeO}_3$  nanoparticles.

*ChemElectroChem* **2014**, *1* (10), 1667–1671.

- [24] Leite, E. R.; Nobre, M. A. L.; Cerqueira, M.; Longo, E.; Varela, J. A., Particle growth during calcination of polycation oxides synthesized by the polymeric precursors method. *Journal of the American Ceramic Society* **1997**, *80* (10), 2649–2657.
- [25] Knoblauch, N.; Dörrer, L.; Fielitz, P.; Schmücker, M.; Borchardt, G., Surface controlled reduction kinetics of nominally undoped polycrystalline CeO<sub>2</sub>. *Physical Chemistry Chemical Physics* **2015**, *17* (8), 5849–5860.
- [26] Deganello, F.; Tummino, M. L.; Calabrese, C.; Testa, M. L.; Avetta, P.; Fabbri, D.; Prevot, A. B.; Montoneri, E.; Magnacca, G., A new, sustainable LaFeO<sub>3</sub> material prepared from biowaste-sourced soluble substances. *New Journal of Chemistry* **2015**, *39* (2), 877–885.
- [27] Thirumalairajan, S.; Giriya, K. M.; Ganesh, V.; Mangalaraj, D.; Viswanathan, C.; Ponpandian, N., Novel synthesis of LaFeO<sub>3</sub> nanostructure dendrites: a systematic investigation of growth mechanism, properties, and biosensing for highly selective determination of neurotransmitter compounds. *Crystal Growth & Design* **2013**, *13* (1), 291–302.
- [28] Wang, K.; Niu, H.; Chen, J.; Song, J.; Mao, C.; Zhang, S.; Zheng, S.;

- Liu, B.; Chen, C., Facile synthesis of CeO<sub>2</sub>–LaFeO<sub>3</sub> perovskite composite and its application for 4–(methylnitrosamino)–1–(3–pyridyl)–1–butanone (NNK) degradation. *Materials* **2016**, *9* (5), 326–337.
- [29] Sudarsanam, P.; Hillary, B.; Mallesham, B.; Rao, B. G.; Amin, M. H.; Nafady, A. Alsalmeh, A. M.; Reddy, B. M.; Bhargava, S. K., Designing CuO<sub>x</sub> nanoparticle–decorated CeO<sub>2</sub> nanocubes for catalytic soot oxidation: role of the nanointerface in the catalytic performance of heterostructured nanomaterials. *Langmuir* **2016**, *32* (9), 2208–2215.
- [30] Lee, K. J.; Kumar, P. A.; Maqbool, M. S.; Rao, K. N.; Song, K. H.; Ha, H. P., Ceria added Sb–V<sub>2</sub>O<sub>5</sub>/TiO<sub>2</sub> catalysts for low temperature NH<sub>3</sub> SCR: physico–chemical properties and catalytic activity. *Applied Catalysis B: Environmental* **2013**, *142–143*, 705–717.
- [31] Ji, K.; Dai, H.; Deng, J.; Song, L.; Xie, S.; Han, W., Glucose–assisted hydrothermal preparation and catalytic performance of porous LaFeO<sub>3</sub> for toluene combustion, *Journal of Solid State Chemistry* **2013**, *199*, 164–170.
- [32] De Asha, A. M.; Critchley, J. T. S.; Nix, R. M., Molecular adsorption characteristics of lanthanum oxide surfaces: the interaction of water with oxide overlayers grown on Cu(111). *Surface Science* **1998**, *405* (2–3), 201–214.

- [33] Zhang, L.; Pierce, J.; Leung, V. L.; Wang, D.; Epling, W. S., Characterization of ceria's interaction with NO<sub>x</sub> and NH<sub>3</sub>. *The Journal of Physical Chemistry C* **2013**, *117* (16), 8282–8289.
- [34] Yang, W.; Zhang, R.; Chen, B.; Duprez, D.; Royer, S., New aspects on the mechanism of C<sub>3</sub>H<sub>6</sub> selective catalytic reduction of NO in the presence of O<sub>2</sub> over LaFe<sub>1-x</sub>(Cu, Pd)<sub>x</sub>O<sub>3-δ</sub> perovskites. *Environmental Science & Technology* **2012**, *46* (20), 11280–11288.
- [35] Han, J.; Meeprasert, J.; Maitarad, P.; Nammuangruk, S.; Shi, L.; Zhang, D., Investigation of the facet-dependent catalytic performance of Fe<sub>2</sub>O<sub>3</sub>/CeO<sub>2</sub> for the selective catalytic reduction of NO with NH<sub>3</sub>. *The Journal of Physical Chemistry C* **2016**, *120* (3), 1523–1533.
- [36] Zhan, S.; Zhu, D.; Yang, S.; Qiu, M.; Li, Y.; Yu, H.; Shen, Z., Sol-gel preparation of mesoporous cerium-doped FeTi nanocatalysts and its SCR activity of NO<sub>x</sub> with NH<sub>3</sub> at low temperature. *Journal of Sol-Gel Science and Technology* **2015**, *73* (2), 443–451.
- [37] Reina, T. R.; Ivanova, S.; Idakiev, V.; Delgado, J. J.; Ivanov, I.; Tabakova, T.; Centeno, M. A.; Odriozola, J. A., Impact of Ce-Fe synergism on the catalytic behaviour of Au/CeO<sub>2</sub>-FeO<sub>x</sub>/Al<sub>2</sub>O<sub>3</sub> for pure H<sub>2</sub> production. *Catalysis Science & Technology* **2013**, *3* (3), 779–787.
- [38] Jiang, T.; Lobo, R. F., On the mechanism of ammonia SCR over Cu-

- and Fe- containing zeolite catalysts. *Structure and Bonding* **2018**, *178*, 155–178.
- [39] Li, Z.; Li, M.; Bian, Z.; Kathiraser, Y.; Kawi, S., Design of highly stable and selective core/yolk-shell nanocatalysts-a review. *Applied Catalysis B: Environmental* **2016**, *188*, 324–341.
- [40] Tian, H.; Huang, F.; Zhu, Y.; Liu, S.; Han, Y.; Jaroniec. M.; Yang, Q.; Liu, H.; Lu, G. Q. M.; Liu, J., The development of yolk-shell-structured Pd&ZnO@carbon submicroreactors with high selectivity and stability. *Advanced Functional Materials* **2018**, *28* (32), 1801737.
- [41] Liu, J.; Qiao, S. Z.; Hartono, S. B.; Lu, G. Q. M., Monodisperse yolk-shell nanoparticles with a hierarchical porous structure for delivery vehicles and nanoreactors. *Angewandte Chemi International Edition* **2010**, *49* (29), 4981–4985.
- [42] Waqif, M.; Bazin, P.; Saur, O.; Lavalley, J. C.; Blanchard. G.; Touret, O., Study of ceria sulfation. *Applied Catalysis B: Environmental* **1997**, *11* (2), 193–205.
- [43] Abdulhamid, H.; Fridell, Erik.; Dawody, J.; Skoglundh, M., *In situ* FTIR study of SO<sub>2</sub> interaction with Pt/BaCO<sub>3</sub>/Al<sub>2</sub>O<sub>3</sub> NO<sub>x</sub> storage catalysts under lean and rich conditions. *Journal of Catalysis* **2006**, *241* (1), 200–210.

- [44] Peña, D. A.; Uphade, B. S.; Reddy, E. P.; Smirniotis, P. G., Identification of surface species on titania-supported manganese, chromium, and copper oxide low-temperature SCR catalysts. *The Journal of Physical Chemistry B* **2004**, *108* (28), 9927–9936.
- [45] Matralis, H. K.; Ciardelli, M.; Ruwet, M.; Grange, P., Vanadia catalysts supported on mixed TiO<sub>2</sub>-Al<sub>2</sub>O<sub>3</sub> supports: effect of composition on the structure and acidity. *Journal of Catalysis* **1995**, *157* (2), 368–379.
- [46] Qin, Y.; Sun, L.; Zhang, D.; Huang, L., Role of ceria in the improvement of SO<sub>2</sub> resistance of La<sub>x</sub>Ce<sub>1-x</sub>FeO<sub>3</sub> catalysts for catalytic reduction of NO with CO. *Catalysis Communications* **2016**, *79*, 53–57.
- [47] Jin, R.; Liu, Y.; Wang, Y.; Cen, W.; Wu, Z.; Wang, H.; Weng, X., The role of cerium in the improved SO<sub>2</sub> tolerance for NO reduction with NH<sub>3</sub> over Mn–Ce/TiO<sub>2</sub> catalyst at low temperature. *Applied Catalysis B: Environmental* **2014**, *148–149*, 582–588.

## 국문 초록

질소산화물( $\text{NO}_x$ )은 질소를 포함하는 연료나 화합물의 연소 과정에서 발생한다. 대기 중으로 유출된 질소산화물은 광화학 스모그, 산성비, 부영양화 등의 다양한 환경문제에 관여함과 동시에 인간에게도 천식과 같은 호흡기질환이나 암을 유발하는 등 직접적인 해를 끼치는 물질이기 때문에 배출에 대한 규제가 세계적으로 강화되고 있다. 선택적 촉매 환원법(Selective Catalytic Reduction,  $\text{NH}_3$ -SCR)은 질소산화물을 제거하는 대표적인 기술 중 하나로, 질소산화물을 환원제인 암모니아와 촉매 반응을 통해 제거하는 기술이다. 반응을 일으키는 촉매는  $\text{NH}_3$ -SCR 공정에서 반응 온도, 효율 등을 결정하는 가장 중요한 요소이며, 현재는 반응 온도에 따라 마나듐, 망간계의 촉매가 주로 사용되고 있다. 하지만 SCR 공정의 촉매는 지속적으로 고온 환경과 이산화황에 노출되기 때문에 이에 따른 내구성 문제가 제기되고 있다. 란탄계 페로브스카이트 촉매는 높은 내구성을 지니고 있어 SCR 공정보다 혹독한 환경에서도 사용되고 있는 물질이다. 하지만 SCR 공정에서의 촉매 효율과 이산화황에 대한 저항능이 매우 낮기 때문에 SCR 촉매로서 활용하기 위해서는

이러한 문제점을 해결할 방법이 필요하다. 본 연구에서는 세륨과 요크-셀 구조를 도입하여 SCR 성능과 이산화황 저항능을 향상시킨 페로브스카이트 촉매를 개발하고자 하였다. SCR 공정에 적합한 세륨 도입 방식을 알아보기 위해 함침, 치환법을 이용하여 도입하였다. X선 회절 분석(XRD)과 주사전자현미경(SE-SEM), 투과전자현미경(TEM) 이미지 분석을 통해 도입된 세륨의 존재 형태를 확인하였다. 치환하여 도입한 샘플이 크게 향상된 SCR 성능을 보였으며, X선 광전자 분광법(XPS) 결과 세륨 치환 샘플에서 촉매 활성화에 영향을 주는  $Ce^{3+}$ 와 표면산소종( $O_s$ ) 비율이 높게 나타난 것이 SCR 성능 향상에 연관된 판단하였다. 함침 샘플에서는 암모니아 흡착을 돕는 역할에 그쳤으나 치환 샘플에서는 결정 내로 들어가 Ce-O-Fe 같은 새로운 활성점을 생성하며 성능을 크게 높인 것으로 확인되었다. 이후 치환 샘플의 합성 과정 중 하소 단계의 승온 속도를 높여 불균일 수축(Heterogeneous contraction) 현상을 활용한 요크-셀 구조 도입을 진행하였다. 결과 세륨이 치환 도입된 샘플에서만 요크-셀 구조가 도입됨을 확인하여 세륨 도입에 의한 조성 변화가 요크-셀 구조 도입에도 영향을 준 것을 알 수 있었다. 요크-셀 구조가 도입된 촉매는 300–450 °C의 온도범위에서 약 90%의 질소산화물

변환 효율을 보이며 세륨과 요크-셀 구조가 도입되지 않은 페로브스카이트 촉매 대비 약 9배의 성능 향상을 달성할 수 있었다. 적외선 분광분석(FT-IR)과 질소산화물 저감 효율을 통해 확인한 이산화황 저항능도 기존 페로브스카이트 촉매 대비 상당히 향상된 것을 확인할 수 있었다. 본 연구의 결과는 기존 SCR 공정에 적합하지 않은 페로브스카이트 촉매를 개선하고 높은 열 안정성을 충분히 활용할 수 있는 새로운 방법이 될 수 있을 것으로 기대된다.